ACS PHYSICAL CHEMISTRY Au
AN OPEN ACCESS JOURNAL OF THE AMERICAN CHEMICAL SOCIETY

pubs.acs.org/physchemau
Article

Lead-Free $Cs_2AgBiCl_6$ Double Perovskite: Experimental and Theoretical Insights into the Self-Trapping for Optoelectronic Applications

Swati N. Rahane, Ganesh K. Rahane, Animesh Mandal, Yogesh Jadhav, Akshat Godha, Avinash Rokade, Shruti Shah, Yogesh Hase, Ashish Waghmare, Nilesh G. Saykar, Anurag Roy, Kranti N. Salgaonkar, Deepak Dubal, Surendra K. Makineni, Nelson Y. Dzade,* Sandesh R. Jadkar,* and Sachin R. Rondiya*

Cite This: ACS Phys. Chem Au 2024, 4, 476−489
Read Online
ACCESS | Metrics & More | Article Recommendations | Supporting Information

ABSTRACT: Lead-free double perovskites (DPs) will emerge as viable and environmentally safe substitutes for Pb-halide perovskites, demonstrating stability and nontoxicity if their optoelectronic property is greatly improved. Doping has been experimentally validated as a powerful tool for enhancing optoelectronic properties and concurrently reducing the defect state density in DP materials. Fundamental understanding of the optical properties of DPs, particularly the self-trapped exciton (STEs) dynamics, plays a critical role in a range of optoelectronic applications. Our study investigates how Fe doping influences the structural and optical properties of $Cs_2AgBiCl_6$ DPs by understanding their STEs dynamics, which is currently lacking in the literature. A combined experimental−computational approach is employed to investigate the optoelectronic properties of pure and doped $Cs_2AgBiCl_6$ (Fe−$Cs_2AgBiCl_6$) perovskites. Successful incorporation of Fe^{3+} ions is confirmed by X-ray diffraction and Raman spectroscopy. Moreover, the Fe−$Cs_2AgBiCl_6$ DPs exhibit strong absorption from below 400 nm up to 700 nm, indicating sub-band gap state transitions originating from surface defects. Photoluminescence (PL) analysis demonstrates a significant enhancement in the PL intensity, attributed to an increased radiative recombination rate and higher STE density. The radiative kinetics and average lifetime are investigated by the time-resolved PL (TRPL) method; in addition, temperature-dependent PL measurements provide valuable insights into activation energy and exciton−phonon coupling strength. Our findings will not only deepen our understanding of charge carrier dynamics associated with STEs but also pave the way for the design of some promising perovskite materials for use in optoelectronics and photocatalysis.

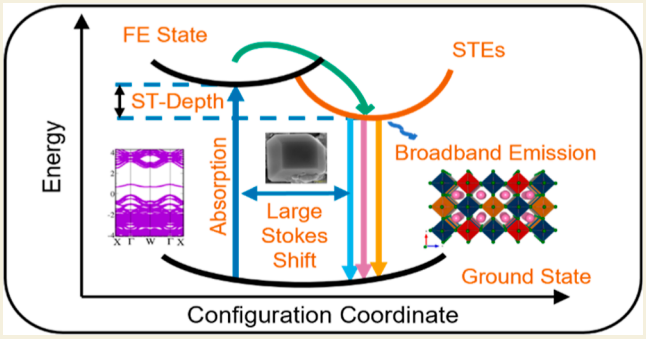

KEYWORDS: *lead-free double perovskites, Fe doping, self-trapped excitons dynamics, $Cs_2AgBiCl_6$, PL and TRPL*

INTRODUCTION

Metal halide perovskites (MHPs) have attracted considerable interest among the scientific community due to their remarkable characteristics. These properties encompass efficient light absorption, extended carrier diffusion lengths and lifetimes, superior charge carrier mobility, robust tolerance to defects, and appropriately positioned band gaps.[1−7] These advantageous electronic and optical characteristics have fueled interest in utilizing MHPs for optoelectronic applications.[8−13] However, the intrinsic instability and toxicity associated with the lead-based perovskite materials pose significant challenges for MHP-based optoelectronic applications, limiting their practical implementation.[4−7] Owing to this, extensive efforts have been dedicated to investigate lead-free and stable alternative halide perovskites that can exhibit photovoltaic and photoelectric properties similar to Pb-based perovskites. Recent findings imply substituting two divalent Pb^{2+} ions in conventional lead halide perovskites (LHPs) with monovalent and trivalent metal ions. This substitution leads to the formation of DP materials. This approach presents a viable solution to address the stability and toxicity concerns while maintaining the three-dimensional (3D) perovskite structure.

To introduce a stable and environmentally friendly metal cation into the perovskite framework, a viable strategy involves incorporating a monovalent metal cation within the lattice. This leads to the creation of a DP structure referred to as elpasolite, characterized by the chemical formula $A_2BB'X_6$. This intriguing

Received: January 30, 2024
Revised: June 8, 2024
Accepted: June 11, 2024
Published: July 5, 2024

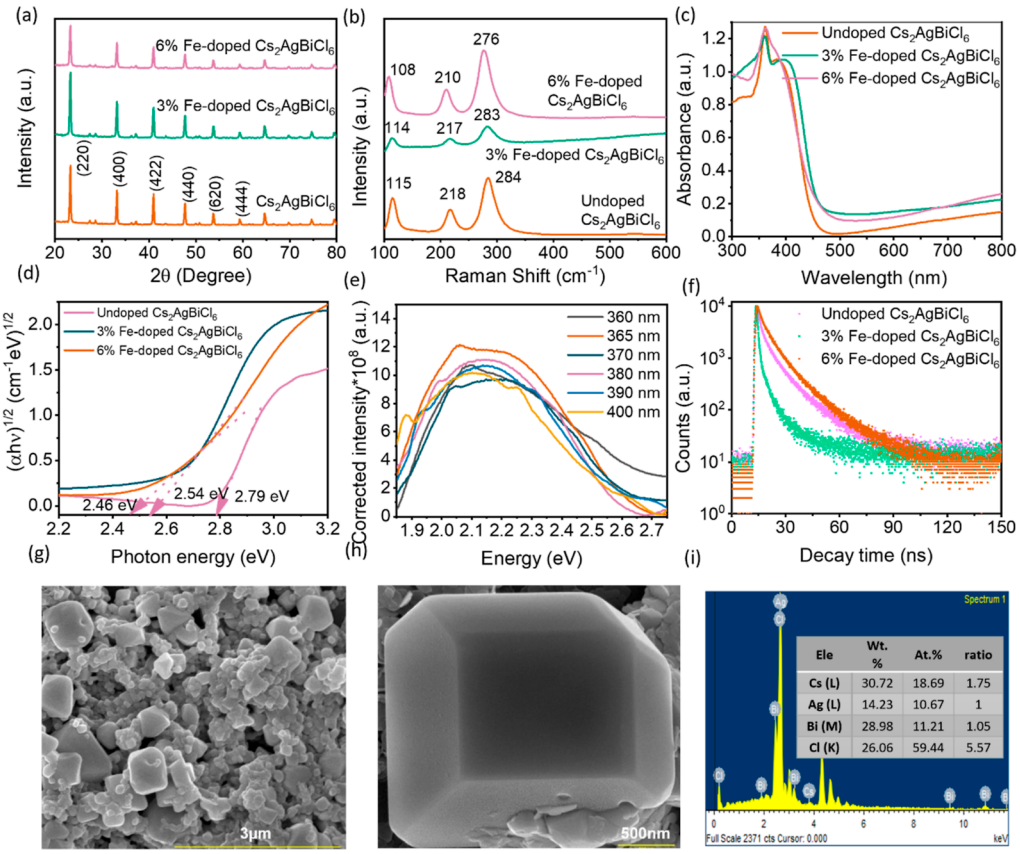

Figure 1. (a) XRD patterns of undoped $Cs_2AgBiCl_6$, 3% Fe− $Cs_2AgBiCl_6$, and 6% Fe−$Cs_2AgBiCl_6$ DPs, (b) Raman spectra of undoped $Cs_2AgBiCl_6$, 3% Fe− $Cs_2AgBiCl_6$, and 6% Fe−$Cs_2AgBiCl_6$ DPs, (c) optical absorption spectra of undoped $Cs_2AgBiCl_6$, 3% Fe− $Cs_2AgBiCl_6$, and 6% Fe−$Cs_2AgBiCl_6$ DPs, (d) Tauc plots used for estimating the band gap of undoped $Cs_2AgBiCl_6$, 3% Fe− $Cs_2AgBiCl_6$, and 6% Fe−$Cs_2AgBiCl_6$ DPs, (e) Jacobian transformed wavelength to energy plots of room-temperature-selective excitation PL spectra of the undoped sample, (f) TRPL traces, (g,h) low- and high-resolution FE-SEM images of undoped $Cs_2AgBiCl_6$, and (i) EDS spectrum recorded for undoped $Cs_2AgBiCl_6$.

and diverse family of perovskites comprises over 350 members, many of which exhibit a 3D crystal structure. Recently, Bismuth (Bi) based halide double perovskites (HDPs) with the formula Cs_2AgBiX_6 (X = Cl and Br) have garnered attention as viable substitutes for lead. These perovskites exhibit a three-dimensional (3D) cubic lattice, featuring metal halide octahedra that share corners, thereby providing substantial compositional versatility.[7,14−17] As Bismuth (Bi) is positioned next to lead (Pb) in the periodic table, it exhibits isoelectronic properties with similarities to lead, including the ability of LHPs to accommodate point defects. Materials containing heavy metal cations that possess a stable pair of valence electrons generally exhibit higher tolerance toward defects.[18] Bismuth, being a stable cation with a large polarizability and $6s^2$ valence electrons, also exhibits a high effective charge, resulting in a high dielectric constant. This attribute is crucial for an increased screening of charged defects.

HDPs have emerged as favorable materials for various uses such as photodetectors, X-ray detectors, photocatalysts, and light-emitting diodes (LEDs).[19−22] Despite considerable efforts to enhance their device performance, the power conversion efficiency of HDP photovoltaic devices remains substantially lower (<2.5%) compared to Pb-based perovskites (>25%).[23−25] The discrepancy suggests the presence of intrinsic electronic limitations and distinctions between the Bi-based and Pb-containing perovskites. A crucial determinant of their performance lies in the pronounced electron−phonon coupling observed in HDPs.[26,27] This coupling enhances carrier scattering, constrains charge carrier mobility, and diminishes photoluminescence quantum yield (PLQY) contributing to undesired electron−hole recombination.[15,28,29] The underlying emission mechanisms in HDPs—whether arising from indirect transitions, defects, or STEs—remain a topic of ongoing scientific discourse.[26,30,31] Consequently, there exists a critical imperative to deepen our comprehension of the electronic structures, characteristics (including band gap), electron−phonon interactions, emission mechanisms, and transport phenomena in HDPs.[32]

Moreover, HDPs exhibit a distinctive ability to emit efficient warm white luminescence via the phenomenon of STEs. STEs correspond to excited states in a material where both the electron and the hole, generated by light absorption, become confined within a localized region or defect in the crystal lattice. The emergence of STEs significantly influences the optical and electronic characteristics of these materials. The confinement of excitons within a localized region modifies their energy levels, emission characteristics, and charge transport behavior in comparison to delocalized excitons. The study and manipulation of STEs hold great significance in the field of optoelectronics as they can influence important phenomena such as PL, charge carrier recombination, and overall device performance. Comprehending and exploiting the emission of STEs in extensively disordered perovskite materials offers intriguing avenues for creating cost-effective and high-performance white light sources.[21,27,33] Introducing an additional element into the DP framework allows for the modulation of optical and

https://doi.org/10.1021/acsphyschemau.4c00008
ACS Phys. Chem Au 2024, 4, 476−489

Table 1. Calculation of Various Parameters for the (220) Plane

sample	diffraction angle, 2θ (degree)	average crystallite size, D (nm)	dislocation density, δ ($\times 10^{14}$) Lines/m^2	strain ε ($\times 10^{-3}$)	interplanar spacing, d (Å)	lattice parameter a (Å)
undoped $Cs_2AgBiCl_6$	23.11	32.04	9.7656	5.0987	3.84	10.86
3% Fe−$Cs_2AgBiCl_6$	23.30	28.65	12.1829	5.6026	3.81	10.78
6% Fe−$Cs_2AgBiCl_6$	23.41	26.30	14.4573	6.3000	3.79	10.73

structural characteristics contingent on the specific chemical composition. Additionally, successful band gap engineering has been achieved by incorporating Mn^{2+}, Sb^{3+}, and In^{3+} ions into the $Cs_2AgBiBr_6$ lattice.[31,34−36] It has been established that doping is a successful strategy for improving the optoelectronic features and decreasing the number of defect states in DPs.

We have reported the successful synthesis of host−dopant pairs using $Cs_2AgBiCl_6$ as the host material and Fe^{3+} as the dopant. The structural, surface, and compositional properties of synthesized nanocrystals (NCs) are meticulously examined using a combination of experimental tools such as X-ray diffraction (XRD), Raman spectroscopy, and X-ray photoelectron spectroscopy (XPS). Investigation of absorption/excitation, recombination processes, and strength of exciton−phonon coupling of the NCs is performed by using PL, TRPL, temperature-dependent PL spectroscopy (TDPL), respectively. Additionally, band alignment studies are carried out by using cyclic voltammetry (CV) measurements to obtain information about band offset.

RESULTS AND DISCUSSION

X-ray Diffraction

These measurements are carried out to study the phase and crystal structures of the synthesized materials. Figure 1a depicts the XRD pattern of both the undoped and Fe− $Cs_2AgBiCl_6$ DPs. The $Cs_2AgBiCl_6$ DP consists of Cs^+ ions positioned in the core of cuboctahedron having alternate $[BiCl_6]^{3-}$ and $[AgCl_6]^{5-}$ octahedral units, resulting in the creation of a three-dimensional grid.[37] XRD pattern of the undoped $Cs_2AgBiCl_6$ has diffraction peaks at $2\theta \sim 23.11$, 33.1, 41.0, 47.62, 53.76, and 59.35° corresponding to the (220), (400), (422), (440), (620), and (444) diffraction planes, respectively. The observed planes correspond to the standard cubic DP arrangement characterized by the $Fm\bar{3}m$ space group and a lattice parameter of approximately 10.79 Å, consistent with prior findings.[14] The average crystallite size, determined by the Scherrer formula, is approximately 32.04 nm for the undoped $Cs_2AgBiCl_6$ DP. As the dopant concentration increases, the diffraction peaks demonstrate a slight shift toward larger diffraction angles, affirming the effective doping of Fe^{3+} ions into the $Cs_2AgBiCl_6$ DP, material which induces a reasonable lattice contraction. No new peaks are observed in the XRD pattern of the doped sample, indicating the absence of impurity phases upon Fe doping. However, higher concentrations of Fe may lead to the formation of impurities. The XRD patterns of all samples reveal multiple peaks, indicating a polycrystalline nature. Also, smaller values of full width at half-maximum (FWHM) of peaks suggest a high level of crystallinity in the synthesized DPs. The average crystallite size of $Cs_2AgBiCl_6$ is decreased slightly upon incorporation of the dopant and is ascribed to the lattice contraction owing to the replacement of larger Bi^{3+} ions (1.03 Å) by smaller Fe^{3+} ions (0.785 Å). The lattice constant contracts from 10.79 Å for the undoped sample to 10.77 and 10.75 Å for 3 and 6% Fe−$Cs_2AgBiCl_6$, respectively. The interplanar spacing (d) estimated from the peak positions of various crystal planes is presented in Table 1 for both the undoped and Fe−$Cs_2AgBiCl_6$ DPs. Notably, Table 1 reveals differences in all structural parameters calculated from XRD for undoped and Fe−$Cs_2AgBiCl_6$ samples. The increasing strain values indicate an elevated level of lattice imperfections with higher dopant concentrations. The dislocation density also increases upon doping, suggesting an increase in the number of imperfections. Conversely, the undoped sample exhibits a low dislocation density, indicating fewer defects. Figure S1 shows the Williamson−Halls plots for each sample. The estimated values of average crystallite size (D), dislocation density (δ), and microstrain (ε) of three samples are listed in Table S4. As observed, the calculated crystallite sizes using the Williamson−Hall technique exceed those obtained through the Scherrer method across all samples. Furthermore, the dislocation density and microstrain values for both undoped and Fe−$Cs_2AgBiCl_6$, as determined by the Williamson−Hall approach, are lower compared to those calculated using the Scherrer equation. Fe^{3+} ions have the potential to incorporate into the $Cs_2AgBiCl_6$ crystal lattice through three plausible mechanisms: substitution for $[BiCl_6]^{3-}$] octahedra, $[AgCl_6]^{5-}$ octahedra, or Cs^+ ions at the A-site. Because of the significant difference in electronegativity between Fe (1.83) and Cs (0.79), along with the mismatch in charge between Fe^{3+} and Cs^+, substituting Cs with Fe ions in the $Cs_2AgBiCl_6$ lattice is improbable. Conversely, Fe's electronegativity closely aligns with that of Ag (1.93) and Bi (2.0), and the charge equilibrium is efficiently maintained by Bi^{3+} and Fe^{3+}, in contrast to the Bi^{3+} and Ag^+ combination. Consequently, it is anticipated that $[FeCl_6]^{3+}$ octahedra will supplant the $[BiCl_6]^{3+}$ octahedra in the Fe−$Cs_2AgBiCl_6$ lattice. The various structural parameters are calculated from XRD for all the diffraction peaks for all three samples and are shown in Tables S1, S2, and S3, respectively.

Raman Spectroscopy

Figure 1b illustrates the Raman spectra of both undoped and Fe−$Cs_2AgBiCl_6$, excited by a 532 nm laser beam. The spectra show three Raman modes for all three samples. The band detected at 115 cm^{-1} represents vibrational motion of Ag−Cl bonds with T_{2g} symmetry. Furthermore, two bands are detectable at 218 cm^{-1} and 284 cm^{-1}, denoting the stretching movements of the $AgCl_6$ octahedron with vibrational symmetries of E_g and A_{1g}, respectively. The longitudinal optical (LO) phonon modes are located at 284 cm^{-1}.[38] When 3% Fe doping is introduced, a slight shift in the peak positions is observed, resulting in modes at 114, 215, and 284 cm^{-1}. Upon increasing the doping concentration to 6%, the Raman peaks undergo further red-shift, resulting in peaks at 108, 210, and 276 cm^{-1}. This shift is primarily attributed to strain/stress lattice distortions or bond length distortion. The decrease in peak intensity can be attributed to lattice compression that resulted from replacing larger Bi^{3+} ions with smaller Fe^{3+} ions. The broadening of the peaks indicates an increase in material defects induced by doping.

https://doi.org/10.1021/acsphyschemau.4c00008
ACS Phys. Chem Au 2024, 4, 476−489

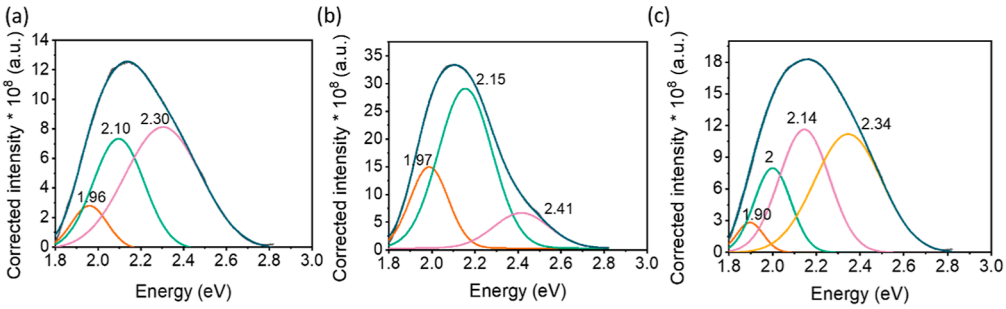

Figure 2. (a–c) Jacobian transformed room-temperature PL spectra of undoped $Cs_2AgBiCl_6$, 3% Fe– $Cs_2AgBiCl_6$, and 6% Fe–$Cs_2AgBiCl_6$ DPs, respectively.

UV–Visible Spectroscopy

To explore the fundamental optical characteristics of as-synthesized perovskites, UV–vis spectroscopy and PL measurements are performed. The optical absorption spectra of both undoped $Cs_2AgBiCl_6$ and Fe–$Cs_2AgBiCl_6$ DPs are depicted in Figure 1c. The absorption spectrum for the undoped $Cs_2AgBiCl_6$ shows a well-defined feature at 365 nm (3.39 nm) and an absorption tail at longer wavelengths. This asymmetric peak lying 0.6 eV above the band gap is identified as a localized Bismuth $6s^2$–$6s^16p^1$ transition, and a long absorption tail which is extended up to 700 nm corresponds to the trap-state-related sub-band gap transition. The linear regions in the absorption spectrum are assigned to a phonon-assisted absorption process. The optical absorption spectra of 3 and 6% Fe–$Cs_2AgBiCl_6$ DPs show a slight shift in the peak position and shape. The absorbance and photon energy are related through equation,

$$(\alpha h\nu)^{1/n} = C^*(h\nu - E_g) \quad (1)$$

where C is the proportionality constant and n is an integer. It is 1/2 for the allowed direct transition and 2 for the allowed indirect transition. The band gap is determined by extending the linear segment of the $(\alpha h\nu)^{1/2}$ versus $h\nu$ plot in the indirect band gap Tauc plot, in which α represents an absorption coefficient and $h\nu$ denotes the incident photon energy. As shown in Figure 1d, the undoped $Cs_2AgBiCl_6$ has an indirect band gap of 2.79 eV, whereas for the 3 and 6% Fe–$Cs_2AgBiCl_6$ DP, the band gap is estimated at 2.54 and 2.46 eV, respectively. The red-shift in the band gap can be ascribed to the interaction between the conduction electrons within the host lattice and the localized d electrons of Fe, which substitutes some of the Bi ions. The extent of this interaction depends on how probable it is for the conduction electrons to collide with localized electrons. Therefore, doping enhances the possibility of collisions, which determines the extent of the red-shift in the band gap. Also, the lattice disorder resulting from the replacement of Bi ions with Fe ions created defect energy states within the band gap. So, the reduction in band gap of the material on doping can be attributed to the doping-induced defective energy levels. To quantify energetic disorder at the band edges of the as-synthesized materials, we have calculated the Urbach energy using the equation,

$$\alpha = \alpha_0 \exp\left(\frac{h\vartheta}{E_u}\right) \quad (2)$$

where α represents an absorption coefficient, Eu denotes Urbach energy, and $h\nu$ stands for incident photon energy. The Urbach value is determined by plotting $\ln(\alpha)$ against the photon energy $(h\nu)$. The inverse of the slope of linear fit provides the Urbach energy value. The Urbach energy for undoped, 3% Fe–$Cs_2AgBiCl_6$, and 6% Fe–$Cs_2AgBiCl_6$ is 99, 145, and 230 meV, respectively. The calculated Urbach energy values confirmed the increased structural distortion in the material with an increasing dopant concentration. The Urbach energy plots and calculated values are listed in Figure S2 and Table S5, respectively.

Photoluminescence

Figure 2 exhibits the Jacobian transformed PL spectra of the undoped and Fe–$Cs_2AgBiCl_6$ DPs at room temperature. A 365 nm excitation wavelength is used for sample excitation. Due to the broad nature of PL peaks in all three samples, we have deconvoluted them. Deconvoluted PL shows presence of three peaks in undoped and 3% Fe–$Cs_2AgBiCl_6$, while the PL of 6% Fe–$Cs_2AgBiCl_6$ shows four peaks, as shown in Figure 2. The emission at ∼2.15 eV arises from band edge excitons. Li et al. reported that the antisite defect Bi_{Ag} is a deep donor defect which is an effective electron trap center, and the peak at ∼2 eV may be attributed to the Bi_{Ag} antisite defect. The peak at ∼1.9 e V in the 6% Fe-sample is due to the chlorine vacancies present in $Cs_2AgBiCl_6$. The emission at ∼2.35 e V is mainly from Cs_{Cl} antisite defect as reported in the literature.[39] The enhanced intensity of the PL peak in the 3% Fe–$Cs_2AgBiCl_6$ sample can be ascribed to an increase in radiative centers resulting from the introduction of dopants, which create defect energy levels within the band gap. Conversely, reduced intensity in the 6% Fe–$Cs_2AgBiCl_6$ sample suggests a higher occurrence of nonradiative transitions and a lower recombination process due to the formation of more trap centers. The intensity of emission is influenced by the density of excitons, and in this case, an increase in free excitons is observed at 3% dopant concentration, correlating with the observed increase in PL intensity. However, emission quenching occurs at higher dopant concentrations (6% Fe–$Cs_2AgBiCl_6$) as the activity sphere of neighboring dopants interferes, leading to a decrease in intensity. The substitution of Bi with Fe introduces donor states close to the upper region of the valence band (VB).[40] The broadband emission obtained for the undoped and Fe–$Cs_2AgBiCl_6$ consists of emission peaks arising from the free excitons, defect states, and localized states. To check whether there is any change in PL peaks with change in excitation energy, we have carried out the selective excitation PL measurements for the undoped $Cs_2AgBiCl_6$ sample. Figure 1e shows the Jacobian transformed selective excitation PL spectra for the undoped $Cs_2AgBiCl_6$. The spectra suggest that there is no change in the PL peak shape with respect to the change in the excitation energy. We have performed PLQY measurements to obtain more information about photophysical characteristics of our samples. The PLQY values determined are 1.290 ± 0.004, 2.260 ± 0.002, and 1.360 ± 0.003, respectively, for the undoped,

https://doi.org/10.1021/acsphyschemau.4c00008
ACS Phys. Chem Au 2024, 4, 476–489

Table 2. Calculation of Average Lifetime from TR-PL Traces

sample	τ_1 (ns)	% contribution	τ_2 (ns)	% contribution	average lifetime t (ns)
undoped $Cs_2AgBiCl_6$	1.73	72.48	9.16	27.52	6.69
3% Fe−$Cs_2AgBiCl_6$	0.85	94.25	6.48	5.75	2.64
6% Fe−$Cs_2AgBiCl_6$	2.85	57.28	10.06	42.72	8.07

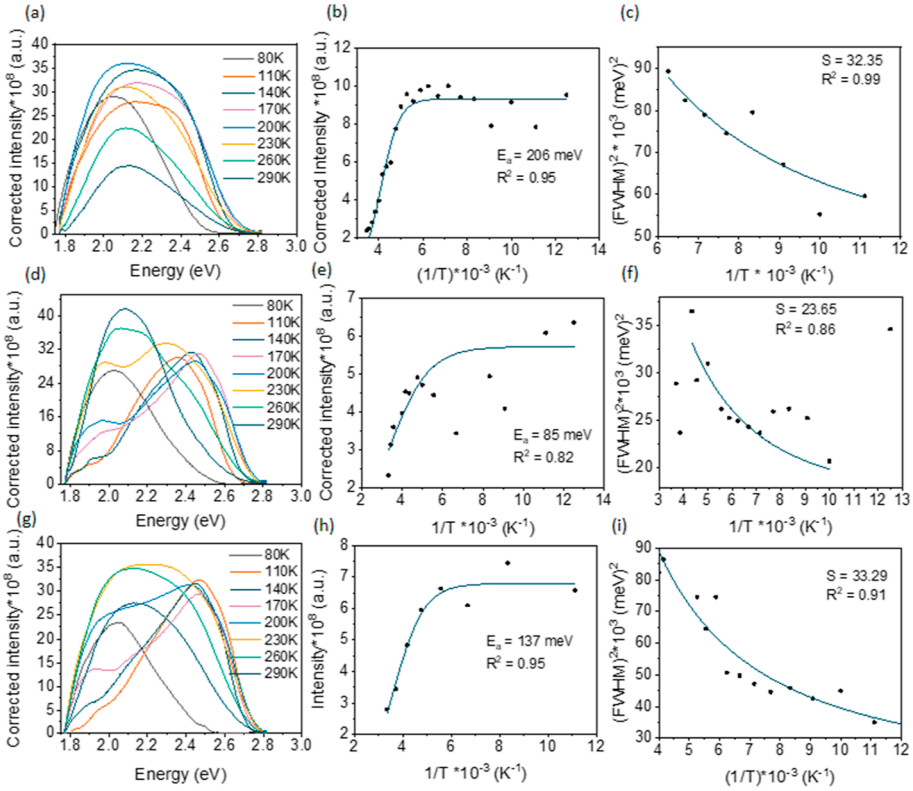

Figure 3. (a,d,g) Jacobian transformed TDPL spectra of undoped $Cs_2AgBiCl_6$ and 3 and 6% Fe−$Cs_2AgBiCl_6$ DPs, respectively (80−300K). (b,e,h) Corrected PL intensity vs $1/T$ curves for undoped $Cs_2AgBiCl_6$ and 3 and 6% Fe−$Cs_2AgBiCl_6$ DPs, respectively. (c,f,i) $(\text{fwhm})^2$ vs $1/T$ curves for undoped $Cs_2AgBiCl_6$, 3% Fe− $Cs_2AgBiCl_6$, and 6% Fe−$Cs_2AgBiCl_6$.

3% Fe−$Cs_2AgBiCl_6$ and 6% Fe−$Cs_2AgBiCl_6$. These values agree with the enhancement in PL intensity with an increase in the dopant concentration from 0 to 3% and again decrease with an increase in concentration to 6%.

Time-Resolved Photoluminescence

The optical properties of the $Cs_2AgBiCl_6$ DP materials are further investigated through TRPL measurements. Figure 1f displays the TRPL of the undoped and Fe−$Cs_2AgBiCl_6$ DP materials, with a laser excitation wavelength of 300 nm. TRPL results revealed a significant reduction in PL lifetime after Fe doping. The effective PL lifetime of undoped $Cs_2AgBiCl_6$ DPs is approximately 6.69 ns, which decreased to 2.64 ns with 3% Fe doping but increased to 8.07 ns with 6% Fe doping. This unusual variation in PL lifetime contradicts the common observation where PL lifetime increases with enhancement in PL intensity, resulting from the suppression of nonradiative relaxation. Consequently, we infer that the observed decrease in the lifetime for 3% Fe−$Cs_2AgBiCl_6$ primarily arises from an augmented radiative decay (or recombination) rate of STEs induced by Fe doping (Table 2). To fit the emission decay curve, the following biexponential function is used.

$$A(t) = A_1 \exp\left(\frac{-t}{\tau_1}\right) + A_2 \exp\left(\frac{-t}{\tau_2}\right) \quad (3)$$

where τ_1 and τ_2 denote decay constants for the fast and slow components, respectively. The biexponential decay signifies two distinct phenomena. The initial fast decay of the PL component arises from the recombination of newly formed excitons, whereas the prolonged decay is assigned to exciton recombination facilitated by the involvement of surface states. The shorter lifetimes in indirect band gap semiconductors are generally due to impurities and defects. The Raman measurements support the TR-PL measurements. The exciton binding energy can be harnessed and efficiently converted into a photocurrent. In crystals, excitons interact with phonons, i.e., lattice vibrations. Before cooling, the electrons strongly interact and can couple to the LO phonons. When electron−lattice interactions are so strong, the electron is expected to create its own hole and become confined within it. If this coupling is weak, then excitons would be scattered by the phonons. Excitons can interact with acoustic phonons, resulting in the formation of STEs. Alternatively, they can initially create self-trapped electrons or holes, which subsequently become Coulombically bound to carriers of opposite charge and form STE. Excitons have the ability to self-trap, thereby localizing energy, which results in variations in the optical characteristics of material. The optoelectronic properties of materials determine whether the self-trapped holes, self-trapped electrons, or STE is formed. In systems with more than two dimensions, an energy barrier exists

https://doi.org/10.1021/acsphyschemau.4c00008
ACS Phys. Chem Au 2024, 4, 476−489

that separates self-trapped states from free-electron states. The self-trapping of excitons is particularly significant as it leads to energy localization, which in turn enables defect processes. In alkali and alkaline-earth halides, the wide conduction band (CB) and high localization energy prevent electron self-trapping. Nevertheless, holes can self-trap, influenced partially by polarization and chemical factors. For example, a hole can bond with two Cl^- ions to create a molecular ion, Cl_2^-. A significant Stokes shift frequently signifies the existence of STEs. Luminescence is influenced by electron−phonon coupling, which broadens emissions through scattering. The absorption and emission of phonons can alter the transition energies that lead to conversion of sharp peaks to wider ones, with electron−phonon coupling strength playing a crucial role. Bismuth-based perovskites exhibit intrinsic self-trapping behavior. TDPL results for these perovskites suggest strong coupling, with STEs being responsible for the broad PL bands. Strong electron−phonon interactions lead to highly localized excited carriers, causing excitons to be immediately trapped by the lattice deformation. The dimensions of any system affect the extent of self-trapping, with lower-dimensional materials exhibiting stronger self-trapping effects.

Exciton binding energy, E_b, varies as m^*/ε, where m^* denotes an effective mass of charge carriers and ε means dielectric constant of material. Higher values of m^* alongside low ε values result in higher E_b value and a more difficult charge separation process for Bismuth perovskites. High E_b values lead to large Stoke's shift between absorption and emission spectra, which describes the magnitude of electron−phonon coupling. Self-trapping can be detected by measuring the PL and TRPL characteristics of the semiconductor across different temperatures. Generally, systems in which self-trapping occurs, the PL exhibits broadening and a Stokes shift relative to the band edge. With this, we calculate Huang−Rhys factor (S) as follows,

$$E_{\text{Stokes}} = 2S\hbar\omega_{\text{LO}} \tag{4}$$

where E_{Stokes} is the measured Stokes shift energy and $\hbar\omega_{\text{LO}}$ is the LO phonon mode energy. The larger value of S indicates that the strength of electron−phonon coupling is more via Frohlich interactions. This means that the STEs can easily form when the S value is higher.

Temperature-Dependent PL Spectroscopy

To understand the effect of band gap (direct or indirect) on the properties of STEs, states of excitons, shallow defects, and the temperature dependence of band gap energy, etc., the TDPL measurements are carried out (Figure 3). The direct band gap materials exhibit bright STE PL while indirect band gap materials exhibit no (dark) STE PL at room temperature.[38] At low temperature (below 270 K), $Cs_2AgBiCl_6$ exhibit broadband PL. The broadband PL of this material can be assigned to STE PL. However, the direct/indirect band gap effect on STE PL is not well understood.[16,31,41−44] The broadband PL is explained by the exciton−phonon coupling-induced self-trapped states.[26,45−47] So we check the exciton−phonon coupling strength of the indirect band gap materials by measuring the TDPL spectra. The change in the fwhm with temperature involves numerous scattering mechanisms, such as interactions among electrons, optical phonons, and acoustic phonons within the material. These interactions cause electrons to shift to a thermal equilibrium position, which thereby affects the electronic band structure and properties of the PL spectra. For the undoped $Cs_2AgBiCl_6$ DPs, as temperature rises from 80 to 300 K, we observed reduced intensity and increased fwhm. The deconvolution of low-temperature PL spectra at three different temperatures (90, 110, and 270 K) for undoped $Cs_2AgBiCl_6$, 3% Fe−$Cs_2AgBiCl_6$, and 6% Fe−$Cs_2AgBiCl_6$ is performed (Figure S4). The nonradiative recombinations are hindered at reduced temperatures, and hence, the enhanced PL intensity is generated. The plot of corrected PL intensity vs $1/T$ is (Figure S5) fitted with $R^2 \sim 1$ using an Arrhenius equation

$$I(T) = \frac{I_0}{1 + A\exp\left(\frac{-E_a}{k_b T}\right)} \tag{5}$$

where $I(T)$ and I_0 denote the corrected intensities of PL peaks at temperatures T and zero K, respectively. A is a constant, k_b is the Boltzmann constant, and E_a stands for activation energy of the nonradiative processes. The activation energy calculated from the above equation is 206 meV for the undoped sample, and it decreased to 85 and 137 meV for the 3 and 6% Fe−$Cs_2AgBiCl_6$ DPs, respectively. The reduction in intensity is related to the broadening of peaks, and this phenomenon is attributable to phonon-assisted carrier recombination of STEs. In all of the three samples, the peak intensity first increased and then decreased. Such variation in intensities is attributed to the capture and release of excitons through thermal activation from STE states.[48] To explore the effect of exciton−phonon coupling, the temperature dependence of peak broadening is studied using the equation[48]

$$\text{FWHM} = 2.36\sqrt{S}\,\hbar\omega_{\text{phonon}}\sqrt{\coth\frac{\hbar\omega_{\text{phonon}}}{2k_b T}} \tag{6}$$

The phonon energy $\hbar\omega_{\text{phonon}}$ and Haung−Rhys parameters calculated by fitting the above equation are 16 and 32.35 meV, respectively, for the undoped sample. For the Fe-doped samples, the phonon energy and Huang−Rhys parameters are 11 meV and 33.29, respectively. The peak positioned at 2.15 eV (main PL feature) is blue-shifted for the temperature range 80−200 K and again shifted to higher wavelengths with further rise in temperature, which is consistent with previous investigations[48] and that can be ascribed to lattice deformation and shifting of VB with temperature. The same trend is observed in the doped samples. The red-shift above 200 K may be attributed to the defect states. As can be seen, the PL is broad and hence deconvolution yields five features located at about 1.92, 2.01, 2.15, 2.37, and 2.54 eV, respectively, for all three samples. The peaks at 1.85, 1.92, and 2.2 eV are due to the STE emission in the undoped sample. For 3% Fe−$Cs_2AgBiCl_6$, the emission at 2.05 eV comes from the STEs. The peaks at 1.9 and 2.3 eV are from V_{Cl} and Cs_{Cl}, respectively.[39] For 6% Fe−$Cs_2AgBiCl_6$ sample, two peaks at 1.9 and 2 eV arise from STEs (Figure S6). The peaks corresponding to 2.40 and 2.50 eV are probably originated due to phase transitions to a tetragonal structure[49] or because of the potential to initiate transitions that are parity-forbidden between the band edges, which can destroy the absorption characteristics of materials,[50] but this is the part of ongoing research and thus needs further investigation. The peaks from STEs disappear at higher temperature in all three samples (Above 270 K). At low temperature, the luminescence came from the host material transition from the self-trapped excitonic state to the ground state. When the temperature increases, the lattice vibrations increase. This facilitates a greater transfer of energy from the host's STE states to the dopant states, and this results in a weak emission from the dopants. No additional peak

https://doi.org/10.1021/acsphyschemau.4c00008
ACS Phys. Chem Au 2024, 4, 476−489

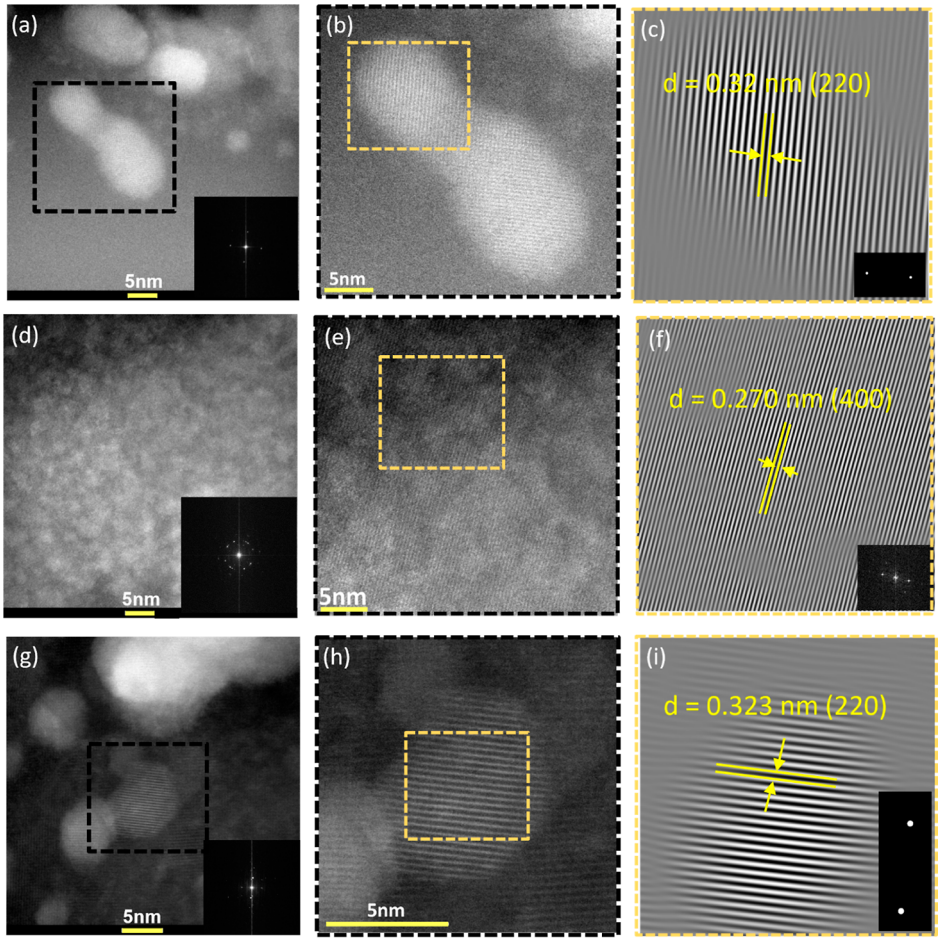

Figure 4. (a,d,g) Low-resolution TEM images of undoped $Cs_2AgBiCl_6$, 3% Fe− $Cs_2AgBiCl_6$, and 6% Fe−$Cs_2AgBiCl_6$ perovskites, respectively. The insets show the corresponding SAED patterns. (b,e,h) HRTEM images of undoped $Cs_2AgBiCl_6$, 3% Fe− $Cs_2AgBiCl_6$, and 6% Fe−$Cs_2AgBiCl_6$ perovskites. (c,f,i) HRTEM images and the insets show the SAED pattern for (220), (400), and (220) planes of undoped $Cs_2AgBiCl_6$, 3% Fe−$Cs_2AgBiCl_6$, and 6% Fe−$Cs_2AgBiCl_6$ perovskites, respectively.

is observed with temperature variations, meaning that there are no temperature-induced phase changes.

Field Emission Scanning Electron Microscopy

Figure 1g,h depicts the FE-SEM images of the undoped sample with varying resolutions. FE-SEM images for 3 and 6% Fe−$Cs_2AgBiCl_6$ at three different resolutions are provided (Figure S7). The images illustrate the crystal formation with dimensions ranging from 1 to 2 μm. A detailed close-up image reveals the presence of perfectly formed dipyramidal units characterized by a cubic crystal system. Energy-dispersive spectroscopy (EDS) is employed for compositional analysis of the $Cs_2AgBiCl_6$ DP. The elemental composition is studied using the EDS technique. EDS spectra are obtained within the energy range of 0−10 eV for the undoped $Cs_2AgBiCl_6$ DP (Figure 1i), 3% Fe−$Cs_2AgBiCl_6$ (Figure S8a), and 6% Fe−$Cs_2AgBiCl_6$ (Figure S8b). The spectrum clearly indicates that the synthesized material exhibits nearly stoichiometric composition. Furthermore, the obtained chemical composition values closely align with the atomic composition of the precursor materials. Notably, the EDS pattern exhibits peaks at 0.7 and 6.4 eV, validating that Fe is present in the lattice.

Transmission Electron Microscopy

The transmission electron microscopy (TEM) images presented in Figure 4a,d,g) exhibit the cubic structure of the undoped, 3% Fe−$Cs_2AgBiCl_6$, and 6% Fe−$Cs_2AgBiCl_6$ DPs, respectively. Additional TEM images at various resolutions for undoped, 3, and 6% Fe−$Cs_2AgBiCl_6$ DPs are shown in the Supporting Information (Figure S9). Notably, the high-resolution TEM (HRTEM) images (Figure 4b,e,h) reveal distinct lattice fringes. Analyzing the TEM data, the interplanar distance derived from the undoped $Cs_2AgBiCl_6$ is approximately 0.32 nm, signifying that the crystal planes correspond to the (220) orientation. Moreover, the polycrystalline materials demonstrate a preferential growth along the (220) direction. The prominent diffraction spots in the selected area electron diffraction (SAED) pattern for all three samples confirm their polycrystalline nature. Moreover, Figure 4c,f,i) shows the zoomed HRTEM images, and the insets show the SAED pattern for (220), (400), and (220) planes of undoped, 3% Fe−$Cs_2AgBiCl_6$, and 6% Fe−$Cs_2AgBiCl_6$ perovskites, respectively.

X-ray Photoelectron Spectroscopy

Identification of elements present in $Cs_2AgBiCl_6$ thin films is determined with the help of XPS measurements. Survey scan XPS for undoped $Cs_2AgBiCl_6$ and for 3% Fe−$Cs_2AgBiCl_6$ are performed (Figure S10). Figure 5 shows the core level XPS for undoped, 3, and 6% Fe−$Cs_2AgBiCl_6$ DPs, respectively. The XPS spectra of Fe−$Cs_2AgBiCl_6$ show the appearance of peaks indicative of Cs 3d, Ag 3d, Bi 4f, Cl 2p, and Fe 2p. Figure 5a−l shows the elemental scan of 3d-Cs, 3d-Ag, 4f-Bi, and 2p-Cl in the

https://doi.org/10.1021/acsphyschemau.4c00008
ACS Phys. Chem Au 2024, 4, 476−489

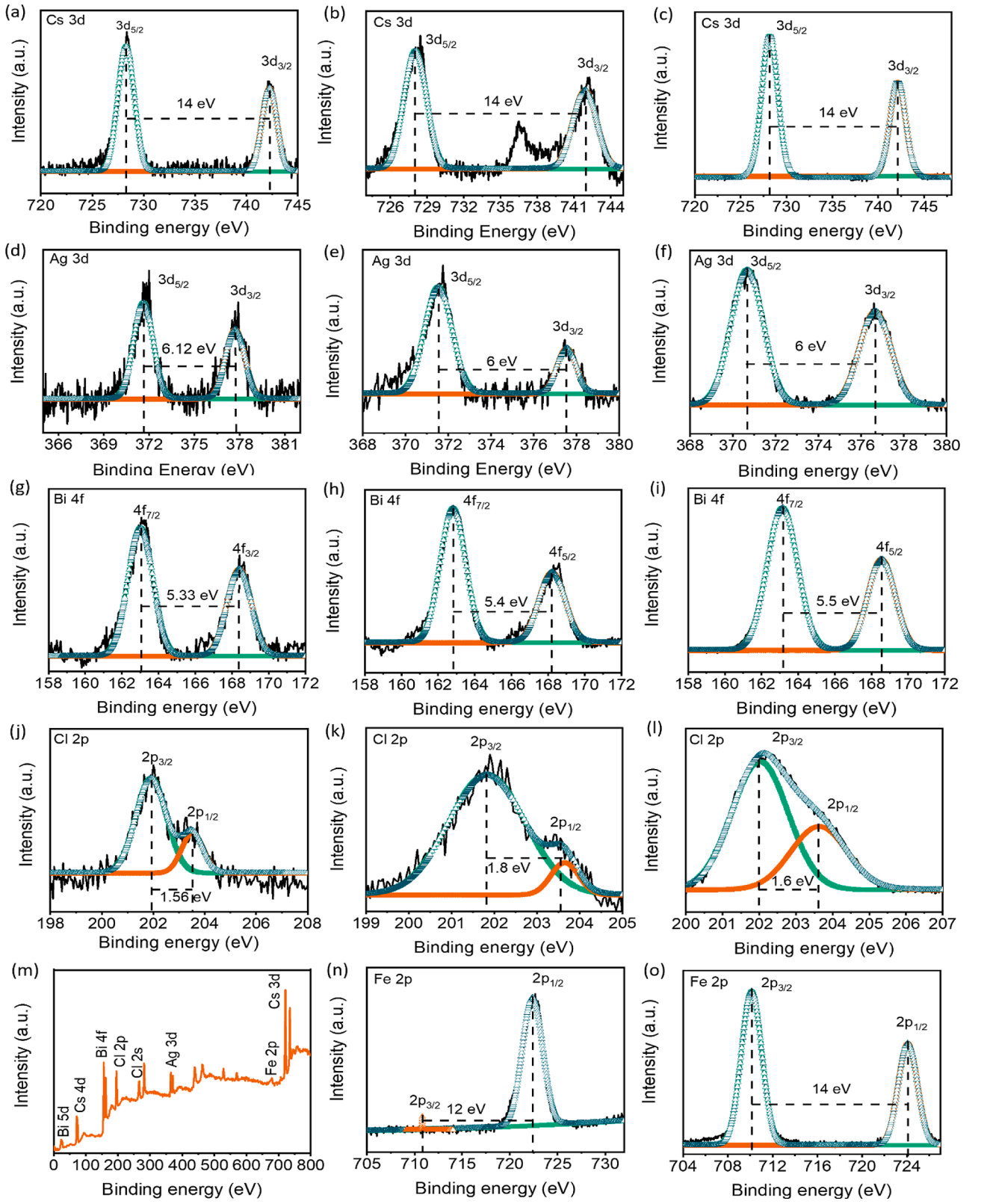

Figure 5. (a–c) Core level XPS for Cs 3d in undoped $Cs_2AgBiCl_6$, 3% Fe– $Cs_2AgBiCl_6$, and 6% Fe–$Cs_2AgBiCl_6$ DPs, respectively. (d–f) Core level XPS for Ag 3d in undoped $Cs_2AgBiCl_6$, 3% Fe– $Cs_2AgBiCl_6$, and 6% Fe–$Cs_2AgBiCl_6$ DPs, respectively. (g–i) Core level XPS for Bi 4f in undoped $Cs_2AgBiCl_6$, 3% Fe– $Cs_2AgBiCl_6$, and 6% Fe–$Cs_2AgBiCl_6$ DPs, respectively. (j–l) Core level XPS for Cl 2p in undoped $Cs_2AgBiCl_6$, 3% Fe–$Cs_2AgBiCl_6$, and 6% Fe–$Cs_2AgBiCl_6$ DPs, respectively. (m) Survey scan XPS spectrum for Fe–$Cs_2AgBiCl_6$. (n,o) Elemental scan XPS for Fe 2p in 3% Fe– $Cs_2AgBiCl_6$ and 6% Fe–$Cs_2AgBiCl_6$ DPs, respectively.

undoped, 3, 6% Fe–$Cs_2AgBiCl_6$, respectively. In Figure 5a, the core level XPS spectrum of Cs 3d in undoped Cs reveals two strong peaks. The peak located at 728.1 eV is from $3d_{5/2}$ Cs while another peak at a binding energy of 742.1 eV is from $3d_{3/2}$ Cs.

https://doi.org/10.1021/acsphyschemau.4c00008
ACS Phys. Chem Au 2024, 4, 476–489

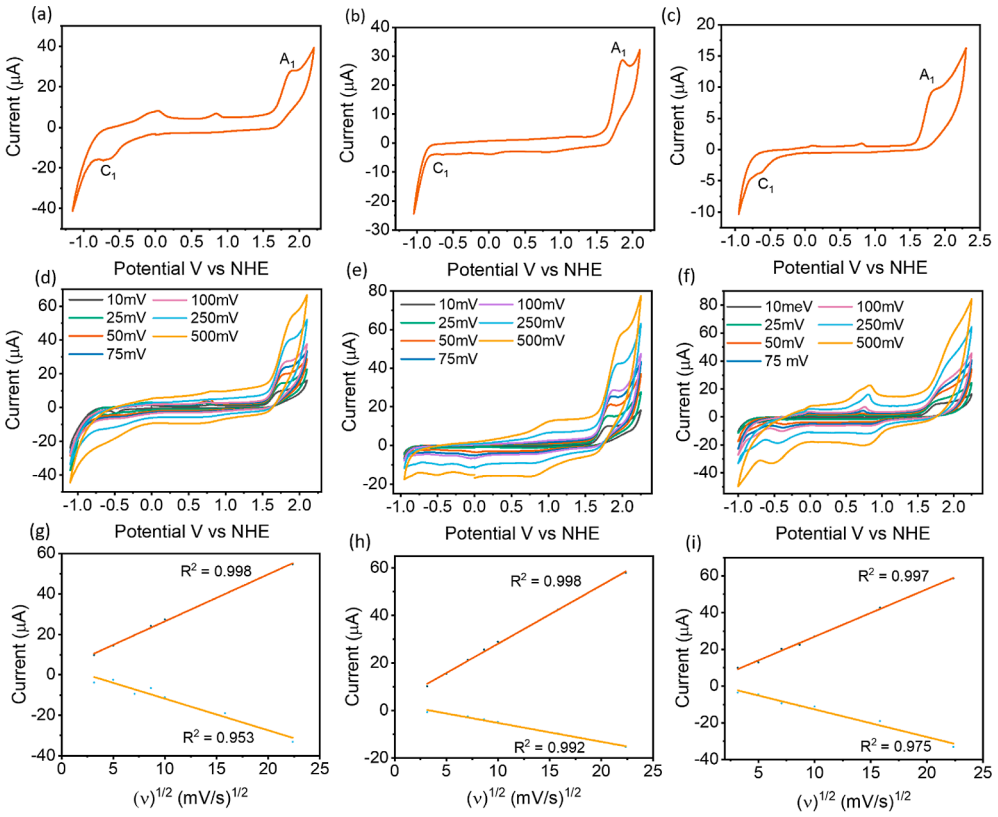

Figure 6. (a–c) Cyclic voltammograms for the undoped $Cs_2AgBiCl_6$, 3% Fe– $Cs_2AgBiCl_6$, and 6% Fe–$Cs_2AgBiCl_6$ for the illustration of the redox behavior as a function of potential applied, (d–f) scan rate-dependent (υ = 10–500 mV) CV responses for the understanding of reaction kinetics in undoped, 3% Fe–$Cs_2AgBiCl_6$, and 6% Fe–$Cs_2AgBiCl_6$, respectively. (g–i) Linear fittings of the scan rate-dependent CV data as square root of scan rate vs current using the Randles–Sevcik equation for undoped $Cs_2AgBiCl_6$, 3% Fe–$Cs_2AgBiCl_6$, and 6% Fe–$Cs_2AgBiCl_6$, respectively.

The elemental scan for 3d-Ag exhibits features at 371.7 and 377.6 eV, corresponding to Ag $3d_{5/2}$ and Ag $3d_{3/2}$, respectively. For Bi, the peaks appear at 163 eV (Bi 4f7/2) and 168.5 eV (Bi 4f5/2), with a shift of 5.5 eV which indicates that Bi is in +3 state. The core level XPS of Cl shows peaks at 202.0 and 203.7 eV, which represent Cl $2p_{3/2}$ and Cl $2p_{1/2}$ states. Figure 5 (n-o) shows an elemental scan of Fe in 3 and 6% Fe–$Cs_2AgBiCl_6$ DP materials, respectively. The Fe peaks are observed at 710.78 and 724.88 eV, representing $2p_{3/2}$ and $2p_{1/2}$ states of Fe. The incorporation of Fe in $Cs_2AgBiCl_6$ DP material is demonstrated by the observed shift in energies toward higher values compared to undoped $Cs_2AgBiCl_6$. This shift indicates a stronger interaction between M (metal) and Cl in the $[BiCl_6]^{3-}$ and $[AgCl]^{5-}$ octahedra, resulting in distinct chemical surroundings for Cs, Ag, and Bi, upon doping. These findings confirm that Fe was effectively doped in $Cs_2AgBiCl_6$. Figure 5m shows the survey scan of the undoped $Cs_2AgBiCl_6$ DP, while the narrow scan spectrum of Cs in 3% Fe–$Cs_2AgBiCl_6$ reveals an additional peak in the range of 730–736 eV, corresponding to the satellite peak of Fe^{3+} ions (Fe $2p_{1/2}$).[51−53]

Electrochemical Measurements

Electronic band structure investigation of synthesized materials is carried out by conducting electrochemical CV measurements. A standard three-electrode system is employed here. The working electrode comprised glassy carbon (GC), while a silver (Ag) wire and a platinum (Pt) loop were utilized as the reference and counter electrodes, respectively. CV measurements are conducted in a 15 mL dichloromethane (DCM) solvent with 100 mM tetrabutylammonium perchlorate (TBAP) as the supporting electrolyte under an inert environment. Prior to the CV measurements, the GC electrode is polished using alumina powder, and the Ag/Pt electrodes are cleaned with dilute nitric acid followed by rinsing with deionized water. Controlled measurements are carried out on the bare electrode in the DCM-TBAP mixture to ensure no redox activity. For preparation of the working electrode, 50 μL (net concentration 1 mg/mL) of the perovskite sample was drop casted followed by vacuum drying.

The obtained cyclic voltammograms for undoped $Cs_2AgBiCl_6$, 3% Fe–$Cs_2AgBiCl_6$, and 6% Fe–$Cs_2AgBiCl_6$ are shown in Figure 6. Prominent anodic and cathodic peak positions are observed at 1.9 and −0.69 V for undoped $Cs_2AgBiCl_6$, 1.86 and −0.65 V for 3% Fe–$Cs_2AgBiCl_6$, and 1.83 and −0.62 V for 6% Fe–$Cs_2AgBiCl_6$. These peaks indicate electrochemical redox reactions occurring at the semiconductor electrode/electrolyte interface, involving between the anodic and cathodic peak potentials, which are charge transfer at specific potentials. The anodic and cathodic peaks represent the extraction and addition of electrons from the band edges of the samples. The electrochemical band gap (E_c) values, determined as difference in the potentials corresponding to the anodic and cathodic peaks resulting from redox reactions occurring at the electrode–electrolyte interface, were observed to be 2.59 eV for undoped $Cs_2AgBiCl_6$, 2.51 eV for 3% Fe– $Cs_2AgBiCl_6$, and 2.45 eV for 6% Fe–$Cs_2AgBiCl_6$. The E_c values align well with the optical band gaps estimated through absorption spectroscopy, which are 2.79, 2.54, and 2.46 eV, respectively. The band edge positions relative to normal hydrogen electrode (NHE) and local vacuum are determined for undoped $Cs_2AgBiCl_6$, 3% Fe–$Cs_2AgBiCl_6$, and 6% Fe–$Cs_2AgBiCl_6$ and are presented in Table

https://doi.org/10.1021/acsphyschemau.4c00008
ACS Phys. Chem Au 2024, 4, 476–489

Table 3. Valence Band (VB) and Conduction Band (CB) Edge Positions vs NHE and Vacuum, Electrochemical Band Gap (E_c) etc. Evaluated Using CV in eV Units

sample	reduction peak (CBM vs NHE)	oxidation peak (VBM vs NHE)	CBM vs vacuum	VBM vs vacuum	electrochemical band gap (eV)
undoped $Cs_2AgBiCl_6$	−0.69	1.9	−3.81	−6.4	2.59
3% Fe−$Cs_2AgBiCl_6$	−0.65	1.86	−3.85	−6.36	2.51
6% Fe−$Cs_2AgBiCl_6$	−0.62	1.83	−3.88	−6.33	2.45

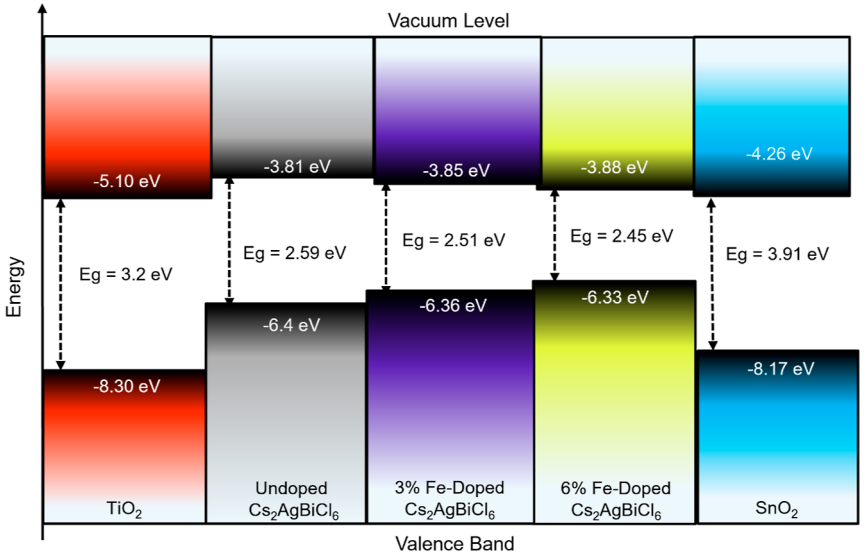

Figure 7. Band alignment diagram of TiO_2, undoped $Cs_2AgBiCl_6$, 3% Fe−$Cs_2AgBiCl_6$, 6% Fe−$Cs_2AgBiCl_6$, and SnO_2, in which CBM and VBM positions vs local vacuum as well as the values of E_c are shown for the respective materials.

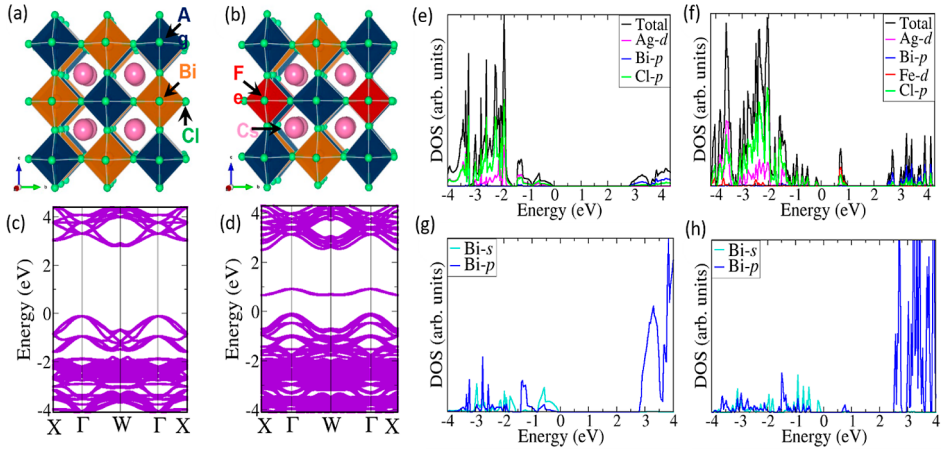

Figure 8. (a) Cubic crystal structure of pristine $Cs_2AgBiCl_6$, (b) Fe−$Cs_2AgBiCl_6$ in polyhedral presentation, (c,d) band structures of $Cs_2AgBiCl_6$ and $Cs_2AgBi_{0.75}Fe_{0.2}5Cl_6$ along high-symmetry directions of the Brillouin zone, and (e,g) PDOS of pristine $Cs_2AgBiCl_6$ and $Cs_2AgBi_{0.75}Fe_{0.25}Cl_6$. Zoomed-in versions are shown in (f,h), respectively.

3. The estimated values align well with those reported by Appadurai et al.[54] To explore the effect of the scan rate on peak current, we recorded cyclic voltammograms (CVs) with progressively increased scan rates for all samples. The recorded CVs are depicted in Figure 6 (d,−f). When the anodic and cathodic peak currents exhibit a direct proportionality with the square root of the scan rate, it indicates a reversible reaction. Conversely, if this relationship does not hold, then it suggests a quasi-reversible reaction. The observed linear relation between the peak current and square root of scan rate for peaks A_1 and C_1, as evidenced by the linear fit, suggests a diffusion-controlled reaction. This finding is supported by previous studies.[55−57] Furthermore, an observable shift in the peak position with an increasing scan rate indicates the presence of kinetic effects.

Figure 7 shows the band alignment diagram of TiO_2, undoped $Cs_2AgBiCl_6$, 3% Fe−$Cs_2AgBiCl_6$, 6% Fe−$Cs_2AgBiCl_6$, and SnO_2, respectively. The figure shows CBM and VBM positions determined for the respective materials vs local vacuum as well as E_c estimated from the CV measurements.

Density Functional Theory Analyses

An additional understanding regarding the structural and electronic properties of the undoped and Fe−$Cs_2AgBiCl_6$ DPs is obtained from analysis of band structures and projected density of states (PDOS) using first-principles density func-

https://doi.org/10.1021/acsphyschemau.4c00008
ACS Phys. Chem Au 2024, 4, 476−489

tional theory (DFT) calculations. Replacement of one Bi^{3+} ion in the undoped cubic $Cs_2AgBiCl_6$ crystal ($Fm3m$ space group) with one Fe^{3+} resulted in the formation of $Cs_2AgBi_{0.75}Fe_{0.25}Cl_6$. Full geometry optimization yields an average cubic lattice parameter of 10.885 Å for undoped $Cs_2AgBiCl_6$ and 10.782 Å for $Cs_2AgBi_{0.75}Fe_{0.25}Cl_6$, indicating that cubic crystalline structure is retained. The reduction in the lattice parameter can be rationalized because a larger Bi^{3+} ion has been partially replaced by a smaller Fe^{3+} ion. From the electronic band diagrams shown in Figure 8, the band gap of the undoped $Cs_2AgBiCl_6$ is predicted at 2.75 eV, which decreased to 2.51 eV with Fe-incorporation ($Cs_2AgBi_{0.75}Fe_{0.25}Cl_6$), in good agreement with the findings from absorption spectroscopy. The dispersive nature of the bands at the VB and CB edges suggests low carrier effective masses that contribute to efficient carrier transport. The electron (hole) effective masses along the X−Γ and Γ−W directions of the Brillouin-zone (Figure 8c,d) are calculated at 0.154 (0.023) and 0.093 (0.083) fractions of m_o (electron rest mass), respectively, for the undoped $Cs_2AgBiCl_6$ and at 0.225 (0.091) and 0.042 (0.061) fractions of m_o (electron rest mass), respectively, for $Cs_2AgBi_{0.75}Fe_{0.25}Cl_6$. The partial replacement of Bi by Fe introduced shallow defect energy levels within the band gap (Figure 8a,b). It is obvious that the VB edge of $Cs_2AgBiCl_6$ and $Cs_2AgBi_{0.75}Fe_{0.25}Cl_6$ is composed mainly of Cl-p and Ag-d orbitals, and the CB edge is primarily governed by Bi-p orbitals. The defect levels introduced below 1.0 eV, are dominated by the Fe-d orbitals, indicating that transition of electrons from the Cl-p state to the Bi-p states would pass through the Fe-d states.

Focusing on Bi s, p-states (Figure 8g,h), the absorption features in $Cs_2AgBiCl_6$ and $Cs_2AgBi_{0.75}Fe_{0.25}Cl_6$ are due to the transition 6s → 6p of the Bi^{3+} ions. The theoretical values for the upper limit of isotropic average electron and hole mobility at room temperature for the undoped $Cs_2AgBiCl_6$ are reported to be 7 and 9 cm^2/Vs, respectively.[49] Although there does not exist any experimental report on the Fe-doping in $Cs_2AgBiCl_6$ underlying effect of doping on carrier mobility, the theoretically reported values are expected to decrease upon Fe-doping due to the increase in the carrier effective masses and the average lifetime of the charge carriers.

CONCLUSIONS

We have successfully synthesized undoped cubic phase $Cs_2AgBiCl_6$ DPs as well as their Fe-doped counterparts using the antisolvent recrystallization method. DFT calculations confirm the retention of the cubic crystalline structure upon Fe doping, while EDS compositional analysis demonstrates that dopants have been uniformly incorporated into the host lattice. Absorption spectra indicate an elongated tail extending up to 700 nm in the Fe−$Cs_2AgBiCl_6$, which indicates that sub-band gap state-related transition may stem from surface defects introduced by dopants. PL measurements exhibit a remarkable enhancement in PL intensity upon Fe doping, attributed to increased radiative rates and the density of free excitons. TDPL analysis yields the higher values of Huang−Rhys parameter (S) indicating strong exciton−phonon coupling, a prerequisite for self-trapping in the material. DFT calculations predict indirect band gaps for both undoped and Fe-doped $Cs_2AgBiCl_6$, with the partial replacement of Bi by Fe introducing shallow defect energy levels within the band gap. The predicted small effective charge carrier masses suggest efficient carrier transport in both undoped and Fe-doped $Cs_2AgBiCl_6$ materials. These findings highlight the potential of Fe-doped $Cs_2AgBiCl_6$ as a phosphor in white LEDs, offering new opportunities for exploring novel lead-free DPs through transition-metal ion doping for diverse applications including solid-state lighting.

EXPERIMENTAL METHODS

Chemicals

Cesium chloride (CsCl, Sigma-Aldrich, 99.00%), silver chloride (AgCl, Sigma-Aldrich, 99.99%), bismuth chloride ($BiCl_3$, Sigma-Aldrich 99.00%), ferric chloride ($FeCl_3$, Sigma-Aldrich, 99.90%), dimethyl sulfoxide (DMSO, Sigma-Aldrich, 99.90%), and 2-propanol (Sigma-Aldrich 99.00%) were used.

Synthesis of $Cs_2AgBiCl_6$ and Fe−$Cs_2AgBiCl_6$ DPs

The undoped and Fe−$Cs_2AgBiCl_6$ DP NCs are synthesized by using the antisolvent method. In the case of pristine samples, a precursor solution is prepared by dissolving 0.2 mmol CsCl (33.67 mg), 0.1 mmol AgCl (14.23 mg), and 0.1 mmol $BiCl_3$ (31.53 mg) in 5 mL of DMSO. Subsequently, 100 μL of the precursor solution is injected into 5 mL of isopropanol with vigorous stirring followed by the centrifugation at 5000 rpm for 5 min to eliminate large crystals and to obtain pristine $Cs_2AgBiCl_6$ crystals. The synthesis of the doped samples (Fe-doped $Cs_2AgBiCl_6$) followed the same procedure as described above, followed by an additional step to add the Fe-precursor to the main precursor solution. The doped samples with Fe doping levels of 3 and 6% in the $Cs_2AgBiCl_6$ DP are prepared by adding 0.006 and 0.012 mmol $FeCl_3$ to the precursor mixture, respectively.

Characterization of $Cs_2AgBiCl_6$ and Fe−$Cs_2AgBiCl_6$ DPs

Structural investigations are conducted by utilizing the XRD technique. A Bruker HR-XRD D8 Adv. instrument with Ni-filtered Cu-Kα radiation at 1.542 Å is employed to obtain diffraction patterns in the θ−2θ scan mode, covering the range of 20−80. Optical absorption spectra of the undoped and Fe−$Cs_2AgBiCl_6$ DPs are acquired in the absorbance mode using a JASCO V-670 UV−visible spectrophotometer. TEM images are obtained using a Titan Themis 300 kV instrument from FEI. The morphology and structure of Fe−$Cs_2AgBiCl_6$ DPs are analyzed using FE-SEM with an FEI Nova NanoSEM 450 instrument. Elemental analysis is performed using EDS with a Bruker X Flash 6130 instrument. Thin films are prepared via drop-casting and spin-coating techniques on glass substrates. XPS measurements are carried out using a PHI 5000 VERSA PROBE III ULVAC PHI instrument (Physical Electronics, USA) to investigate the chemical environment/state of each element (Cs, Ag, Bi, Cl, and Fe). Monochromatic Al K_α radiation at 1486.6 eV is employed as the X-ray source. The base vacuum of the XPS chamber is maintained at a level above 10^{-9} Torr. The carbon corrections are carried out to check peak shifts for each element. Room-temperature PL measurements are conducted using the Fluorolog HORIBA scientific setup. For low-temperature PL measurements, the JANIS (model no. VNF-10) PL setup is employed. Lifetime measurements are performed by utilizing a HORIBA Fluorolog spectrofluorometer equipped with a 300 nm NanoLED laser diode, capable of generating pulse widths of less than 1 ns. CV measurements are conducted using an electrochemical workstation, specifically the Metrohm Potentiostat/Galvanostat Autolab PGSTAT 302N. The PLQY of the films was measured by the integrating sphere method at CSIR-NCL, India. An intensity-modulated 300 w Xe-lamp light source was employed for excitation. First, we measured the blank sample and then subtracted the absorption effect of polymer films while calculating the PLQY. All the PLQY measurements were carried out in air at room temperature.

Computational Details

The DFT computations are carried out using the projector augmented wave technique as incorporated within the Vienna Ab initio Simulation Package (VASP).[58−62] The Perdew−Burke−Ernzerhof functional[63] combined with the Grimme's dispersion correction method[64] are used for geometry optimizations, whereas the screened hybrid functional HSE06 with 25% Hartree−Fock exchange is used for electronic band structure and PDOS calculations.[65] The cutoff energy for the plane wave functions is established at 600 eV, while the threshold for the total

https://doi.org/10.1021/acsphyschemau.4c00008
ACS Phys. Chem Au 2024, 4, 476−489

energy change is set at 10^{-6} eV. Both atomic positions and lattice volume are relaxed using a conjugate-gradient algorithm.[66] The structures are visualized using VESTA software. The pristine and Fe-doped $Cs_2AgBiCl_6$ DPs are modeled in cubic structure ($Fm3m$ space group). A 3 × 3 × 3 Monkhorst−Pack[66] k-point mesh is used in geometry optimization, and a higher k-point mesh of 5 × 5 × 5 is used for electronic structure calculations. From the predicted band diagram, the effective masses of electrons (m_e^*) and holes (m_h^*), which dictate charge transport in the pristine and Fe-doped $Cs_2AgBiCl_6$ DPs are calculated along different Brillouin-zone directions using the relation $m^*_{e(h)} = \pm \hbar^2 \left(\frac{d^2E_k}{dk^2}\right)^{-1}$, where E_k is the energy of the band as a function of the wave vector k and $\hbar$ is the reduced Planck's constant.

■ ASSOCIATED CONTENT

Supporting Information

The Supporting Information is available free of charge at https://pubs.acs.org/doi/10.1021/acsphyschemau.4c00008.

WH analysis plot for all three samples; Urbach energy plot; Jacobian transformed wavelength to energy plots of room-temperature PL spectra of undoped $Cs_2AgBiCl_6$, 3% Fe−$Cs_2AgBiCl_6$, and 6% Fe−$Cs_2AgBiCl_6$ DPs; Jacobian transformed low-temperature PL plot for all three samples at different temperatures; corrected intensity of PL peak vs $1/T$ plot (Arrhenius function) for 6% Fe−$Cs_2AgBiCl_6$ DPs; transition energy levels for intrinsic donor (blue lines) and acceptor (red lines) defects in $Cs_2AgBiCl_6$; FE-SEM images for all three samples at different resolutions; EDS spectra for two doped samples; TEM images for all three samples with various resolutions; survey scan XPS spectra for all three samples; various calculated parameters from XRD patterns of all three samples; comparison of structural parameters derived from the Scherrer Formula and $W-H$ Plots across all samples; and band gap and Urbach energy values calculated from optical absorption spectroscopy (PDF)

■ AUTHOR INFORMATION

Corresponding Authors

Nelson Y. Dzade − *Department of Energy and Mineral Engineering, Pennsylvania State University, University Park, Pennsylvania 16802, United States;* Present Address: Department of Energy and Mineral Engineering, Pennsylvania State University, University Park, PA 16802, United States; orcid.org/0000-0001-7733-9473; Email: nxd5313@psu.edu

Sandesh R. Jadkar − *Department of Physics, Savitribai Phule Pune University, Pune 411007, India;* Present Address: Department of Physics, Savitribai Phule Pune University, Pune 411007, India.; Email: sandesh@physics.unipune.ac.in

Sachin R. Rondiya − *Department of Materials Engineering, Indian Institute of Science, Bangalore 560012, India;* Present Address: Department of Materials Engineering, Indian Institute of Science, Bangalore 560012, India.; orcid.org/0000-0003-1350-1237; Email: rondiya@iisc.ac.in

Authors

Swati N. Rahane − *Department of Physics, Savitribai Phule Pune University, Pune 411007, India*

Ganesh K. Rahane − *Department of Materials Engineering, Indian Institute of Science, Bangalore 560012, India*

Animesh Mandal − *Department of Materials Engineering, Indian Institute of Science, Bangalore 560012, India*

Yogesh Jadhav − *Symbiosis Center for Nanoscience and Nanotechnology (SCNN), Symbiosis International (Deemed University) (SIU), Lavale, Pune 412115 Maharashtra, India*

Akshat Godha − *Department of Materials Engineering, Indian Institute of Science, Bangalore 560012, India*

Avinash Rokade − *Department of Physics, Savitribai Phule Pune University, Pune 411007, India*

Shruti Shah − *Department of Physics, Savitribai Phule Pune University, Pune 411007, India*

Yogesh Hase − *Department of Physics, Savitribai Phule Pune University, Pune 411007, India*

Ashish Waghmare − *Department of Physics, Savitribai Phule Pune University, Pune 411007, India*

Nilesh G. Saykar − *Department of Materials Engineering, Indian Institute of Science, Bangalore 560012, India;* orcid.org/0000-0001-7707-2190

Anurag Roy − *Solar Energy Research Group, Environment and Sustainability Institute, University of Exeter, Penryn Campus, Cornwall TR10 9FE, U.K.;* orcid.org/0000-0002-2097-9442

Kranti N. Salgaonkar − *Catalysis and Inorganic Chemistry Division, CSIR-National Chemical Laboratory, Pune 411008, India; Academic of Scientific and Innovative Research (AcSIR), Pune 411008, India;* orcid.org/0000-0003-1968-1320

Deepak Dubal − *School of Chemistry and Physics, Queensland University of Technology (QUT), Brisbane, Queensland 4000, Australia; Centre for Materials Science, Queensland University of Technology (QUT), Brisbane, Queensland 4000, Australia;* orcid.org/0000-0002-2337-676X

Surendra K. Makineni − *Department of Materials Engineering, Indian Institute of Science, Bangalore 560012, India*

Complete contact information is available at: https://pubs.acs.org/10.1021/acsphyschemau.4c00008

Notes

The authors declare no competing financial interest.

■ ACKNOWLEDGMENTS

S.N.R. and K.N.S. express gratitude to the Chhatrapati Shahu Maharaj Research Training and Human Development Institute (SARTHI) for their generous financial assistance. S.S., Y.H., and A.W. extend their appreciation to the Ministry of New and Renewable Energy (MNRE), Government of India, for their financial support through the National Renewable Energy Fellowship (NREF) program. G.K.R. and S.R.R. acknowledge the support of the Department of Materials Engineering, Indian Institute of Science (IISc), Bangalore, India. S.R.R. acknowledges the Science and Engineering Research Board (SERB), Govt. of India for funding (grant no. EEQ/2022/000697). N.Y.D. acknowledges the valuable Seed Grant provided by the Institute for Computational and Data Sciences at the Pennsylvania State University. The computational aspects of this research are carried out utilizing the computing resources of the Roar supercomputer at the Institute for Computational and Data Sciences, Pennsylvania State University. S.R.R. is thankful to the Advance Facility for Microscopy and Microanalysis (AFMM) at IISc for their support in utilizing microscopy techniques. S.R.R. is also thankful to the Central Instrumenta-

tion Facility, Savitribai Phule Pune University for FE-SEM Facility.

REFERENCES

(1) Eperon, G. E.; Leijtens, T.; Bush, K. A.; Prasanna, R.; Green, T.; Wang, J. T. W.; McMeekin, D. P.; Volonakis, G.; Milot, R. L.; May, R.; Palmstrom, A.; Slotcavage, D. J.; Belisle, R. A.; Patel, J. B.; Parrott, E. S.; Sutton, R. J.; Ma, W.; Moghadam, F.; Conings, B.; Babayigit, A.; Boyen, H. G.; Bent, S.; Giustino, F.; Herz, L. M.; Johnston, M. B.; McGehee, M. D.; Snaith, H. J. Perovskite-Perovskite Tandem Photovoltaics with Optimized Band Gaps. *Science* **2016**, *354* (6314), 861−865.

(2) Jeon, N. J.; Noh, J. H.; Yang, W. S.; Kim, Y. C.; Ryu, S.; Seo, J.; Seok, S. I. Compositional Engineering of Perovskite Materials for High-Performance Solar Cells. *Nature* **2015**, *517* (7535), 476−480.

(3) Tsai, H.; Nie, W.; Blancon, J. C.; Stoumpos, C. C.; Asadpour, R.; Harutyunyan, B.; Neukirch, A. J.; Verduzco, R.; Crochet, J. J.; Tretiak, S.; Pedesseau, L.; Even, J.; Alam, M. A.; Gupta, G.; Lou, J.; Ajayan, P. M.; Bedzyk, M. J.; Kanatzidis, M. G.; Mohite, A. D. High-Efficiency Two-Dimensional Ruddlesden-Popper Perovskite Solar Cells. *Nature* **2016**, *536* (7616), 312−316.

(4) Buin, A.; Pietsch, P.; Xu, J.; Voznyy, O.; Ip, A. H.; Comin, R.; Sargent, E. H. Materials Processing Routes to Trap-Free Halide Perovskites. *Nano Lett.* **2014**, *14* (11), 6281−6286.

(5) Li, F.; Pei, Y.; Xiao, F.; Zeng, T.; Yang, Z.; Xu, J.; Sun, J.; Peng, B.; Liu, M. Tailored Dimensionality to Regulate the Phase Stability of Inorganic Cesium Lead Iodide Perovskites. *Nanoscale* **2018**, *10* (14), 6318−6322.

(6) Feng, G.; Guo, X.; Li, F.; Liao, Y.; Hou, Y.; Liu, M. A Practical Method for Fabricating Perovskite Solar Cells with Remarkable Water Resistance: Via Additive Engineering. *Mol. Syst. Des. Eng.* **2018**, *3* (5), 729−733.

(7) Chen, M.; Ju, M. G.; Garces, H. F.; Carl, A. D.; Ono, L. K.; Hawash, Z.; Zhang, Y.; Shen, T.; Qi, Y.; Grimm, R. L.; Pacifici, D.; Zeng, X. C.; Zhou, Y.; Padture, N. P. Highly Stable and Efficient All-Inorganic Lead-Free Perovskite Solar Cells with Native-Oxide Passivation. *Nat. Commun.* **2019**, *10* (1), 16.

(8) Zhang, H.; Li, W.; Zhang, X.; Yu, C.; Li, T.; Zhang, X.; Gao, Z.; Xiong, C.; Wang, T. Quasi-2D Bromide Perovskite Nanocrystals with Narrow Phase Distribution Prepared Using Ternary Organic Cations for Sky-Blue Light-Emitting Diodes. *Appl. Phys. Lett.* **2021**, *118* (8), 083302.

(9) Sutherland, B. R.; Sargent, E. H. Perovskite Photonic Sources. *Nat. Photonics* **2016**, *10* (5), 295−302.

(10) Lin, Y. H.; Huang, W.; Pattanasattayavong, P.; Lim, J.; Li, R.; Sakai, N.; Panidi, J.; Hong, M. J.; Ma, C.; Wei, N.; Wehbe, N.; Fei, Z.; Heeney, M.; Labram, J. G.; Anthopoulos, T. D.; Snaith, H. J. Deciphering Photocarrier Dynamics for Tuneable High-Performance Perovskite-Organic Semiconductor Heterojunction Phototransistors. *Nat. Commun.* **2019**, *10* (1), 4475.

(11) Dou, L.; Yang, Y. M.; You, J.; Hong, Z.; Chang, W. H.; Li, G.; Yang, Y. Solution-Processed Hybrid Perovskite Photodetectors with High Detectivity. *Nat. Commun.* **2014**, *5*, 5404.

(12) Domanski, K.; Tress, W.; Moehl, T.; Saliba, M.; Nazeeruddin, M. K.; Grätzel, M. Working Principles of Perovskite Photodetectors: Analyzing the Interplay between Photoconductivity and Voltage-Driven Energy-Level Alignment. *Adv. Funct. Mater.* **2015**, *25* (44), 6936−6947.

(13) Guo, Y.; Liu, C.; Tanaka, H.; Nakamura, E. Air-Stable and Solution-Processable Perovskite Photodetectors for Solar-Blind UV and Visible Light. *J. Phys. Chem. Lett.* **2015**, *6* (3), 535−539.

(14) McClure, E. T.; Ball, M. R.; Windl, W.; Woodward, P. M. Cs2AgBiX6 (X = Br, Cl): New Visible Light Absorbing, Lead-Free Halide Perovskite Semiconductors. *Chem. Mater.* **2016**, *28* (5), 1348−1354.

(15) Yang, B.; Chen, J.; Yang, S.; Hong, F.; Sun, L.; Han, P.; Pullerits, T.; Deng, W.; Han, K. Lead-Free Silver-Bismuth Halide Double Perovskite Nanocrystals. *Angew. Chem.* **2018**, *130* (19), 5457−5461.

(16) Yang, B.; Mao, X.; Hong, F.; Meng, W.; Tang, Y.; Xia, X.; Yang, S.; Deng, W.; Han, K. Lead-Free Direct Band Gap Double-Perovskite Nanocrystals with Bright Dual-Color Emission. *J. Am. Chem. Soc.* **2018**, *140* (49), 17001−17006.

(17) Du, K. Z.; Meng, W.; Wang, X.; Yan, Y.; Mitzi, D. B. Bandgap Engineering of Lead-Free Double Perovskite Cs2AgBiBr6 through Trivalent Metal Alloying. *Angew. Chem., Int. Ed.* **2017**, *56* (28), 8158−8162.

(18) Brandt, R. E.; Stevanović, V.; Ginley, D. S.; Buonassisi, T. Identifying Defect-Tolerant Semiconductors with High Minority-Carrier Lifetimes: Beyond Hybrid Lead Halide Perovskites. *MRS Commun.* **2015**, *5* (2), 265−275.

(19) Steele, J. A.; Pan, W.; Martin, C.; Keshavarz, M.; Debroye, E.; Yuan, H.; Banerjee, S.; Fron, E.; Jonckheere, D.; Kim, C. W.; Baekelant, W.; Niu, G.; Tang, J.; Vanacken, J.; Van der Auweraer, M.; Hofkens, J.; Roeffaers, M. B. J. Photophysical Pathways in Highly Sensitive Cs2AgBiBr6 Double-Perovskite Single-Crystal X-Ray Detectors. *Adv. Mater.* **2018**, *30* (46), No. e1804450.

(20) Pan, W.; Wu, H.; Luo, J.; Deng, Z.; Ge, C.; Chen, C.; Jiang, X.; Yin, W. J.; Niu, G.; Zhu, L.; Yin, L.; Zhou, Y.; Xie, Q.; Ke, X.; Sui, M.; Tang, J. Cs2AgBiBr6 Single-Crystal X-Ray Detectors with a Low Detection Limit. *Nat. Photonics* **2017**, *11* (11), 726−732.

(21) Luo, J.; Wang, X.; Li, S.; Liu, J.; Guo, Y.; Niu, G.; Yao, L.; Fu, Y.; Gao, L.; Dong, Q.; Zhao, C.; Leng, M.; Ma, F.; Liang, W.; Wang, L.; Jin, S.; Han, J.; Zhang, L.; Etheridge, J.; Wang, J.; Yan, Y.; Sargent, E. H.; Tang, J. Efficient and Stable Emission of Warm-White Light from Lead-Free Halide Double Perovskites. *Nature* **2018**, *563* (7732), 541−545.

(22) Zhou, L.; Xu, Y. F.; Chen, B. X.; Kuang, D. B.; Su, C. Y. Synthesis and Photocatalytic Application of Stable Lead-Free Cs2AgBiBr6 Perovskite Nanocrystals. *Small* **2018**, *14* (11), 1703762.

(23) Greul, E.; Petrus, M. L.; Binek, A.; Docampo, P.; Bein, T. Highly Stable, Phase Pure Cs2AgBiBr6 Double Perovskite Thin Films for Optoelectronic Applications. *J. Mater. Chem. A* **2017**, *5* (37), 19972−19981.

(24) Pantaler, M.; Cho, K. T.; Queloz, V. I. E.; García Benito, I.; Fettkenhauer, C.; Anusca, I.; Nazeeruddin, M. K.; Lupascu, D. C.; Grancini, G. Hysteresis-Free Lead-Free Double-Perovskite Solar Cells by Interface Engineering. *ACS Energy Lett.* **2018**, *3* (8), 1781−1786.

(25) Ning, W.; Wang, F.; Wu, B.; Lu, J.; Yan, Z.; Liu, X.; Tao, Y.; Liu, J. M.; Huang, W.; Fahlman, M.; Hultman, L.; Sum, T. C.; Gao, F. Long Electron-Hole Diffusion Length in High-Quality Lead-Free Double Perovskite Films. *Adv. Mater.* **2018**, *30* (20), No. e1706246.

(26) Steele, J. A.; Puech, P.; Keshavarz, M.; Yang, R.; Banerjee, S.; Debroye, E.; Kim, C. W.; Yuan, H.; Heo, N. H.; Vanacken, J.; Walsh, A.; Hofkens, J.; Roeffaers, M. B. J. Giant Electron-Phonon Coupling and Deep Conduction Band Resonance in Metal Halide Double Perovskite. *ACS Nano* **2018**, *12* (8), 8081−8090.

(27) Kentsch, R.; Scholz, M.; Horn, J.; Schlettwein, D.; Oum, K.; Lenzer, T. Exciton Dynamics and Electron-Phonon Coupling Affect the Photovoltaic Performance of the Cs2AgBiBr6 Double Perovskite. *J. Phys. Chem. C* **2018**, *122* (45), 25940−25947.

(28) Wright, A. D.; Verdi, C.; Milot, R. L.; Eperon, G. E.; Pérez-Osorio, M. A.; Snaith, H. J.; Giustino, F.; Johnston, M. B.; Herz, L. M. Electron-Phonon Coupling in Hybrid Lead Halide Perovskites. *Nat. Commun.* **2016**, *7*, 11755.

(29) Zhu, X. Y.; Podzorov, V. Charge Carriers in Hybrid Organic-Inorganic Lead Halide Perovskites Might Be Protected as Large Polarons. *J. Phys. Chem. Lett.* **2015**, *6* (23), 4758−4761.

(30) Hoye, R. L. Z.; Eyre, L.; Wei, F.; Brivio, F.; Sadhanala, A.; Sun, S.; Li, W.; Zhang, K. H. L.; MacManus-Driscoll, J. L.; Bristowe, P. D.; Friend, R. H.; Cheetham, A. K.; Deschler, F. Fundamental Carrier Lifetime Exceeding 1 μs in $Cs_2AgBiBr_6$ Double Perovskite. *Adv. Mater. Interfaces* **2018**, *5* (15), 1800464.

(31) Volonakis, G.; Filip, M. R.; Haghighirad, A. A.; Sakai, N.; Wenger, B.; Snaith, H. J.; Giustino, F. Lead-Free Halide Double Perovskites via Heterovalent Substitution of Noble Metals. *J. Phys. Chem. Lett.* **2016**, *7* (7), 1254−1259.

(32) Schade, L.; Wright, A. D.; Johnson, R. D.; Dollmann, M.; Wenger, B.; Nayak, P. K.; Prabhakaran, D.; Herz, L. M.; Nicholas, R.; Snaith, H. J.; Radaelli, P. G. Structural and Optical Properties of Cs 2 AgBiBr 6 Double Perovskite. *ACS Energy Lett.* **2019**, *4* (1), 299−305.

https://doi.org/10.1021/acsphyschemau.4c00008
ACS Phys. Chem Au 2024, 4, 476−489

(33) Hu, M.; Luo, J.; Li, S.; Liu, J.; Li, J.; Tan, Z.; Niu, G.; Wang, Z.; Tang, J. Broadband Emission of Double Perovskite Cs 2 Na 04 Ag 06 In 0995 Bi 0005 Cl 6:Mn 2+ for Single-Phosphor White-Light-Emitting Diodes. *Opt. Lett.* **2019**, *44* (19), 4757.
(34) Vargas, B.; Ramos, E.; Pérez-Gutiérrez, E.; Alonso, J. C.; Solis-Ibarra, D. A Direct Bandgap Copper-Antimony Halide Perovskite. *J. Am. Chem. Soc.* **2017**, *139* (27), 9116−9119.
(35) Chen, N.; Cai, T.; Li, W.; Hills-Kimball, K.; Yang, H.; Que, M.; Nagaoka, Y.; Liu, Z.; Yang, D.; Dong, A.; et al. Yb-and Mn-Doped Lead-Free Double Perovskite Cs2AgBiX6 (X= Cl-Br-) Nanocrystals. *ACS Appl. Mater. Interfaces* **2019**, *11* (18), 16855−16863. others
(36) Shamsi, J.; Urban, A. S.; Imran, M.; De Trizio, L.; Manna, L. Metal Halide Perovskite Nanocrystals: Synthesis, Post-Synthesis Modifications, and Their Optical Properties. *Chem. Rev.* **2019**, *119* (5), 3296−3348.
(37) Xiao, Z.; Du, K. Z.; Meng, W.; Wang, J.; Mitzi, D. B.; Yan, Y. Intrinsic Instability of Cs2In(I)M(III)X6 (M = Bi, Sb; X = Halogen) Double Perovskites: A Combined Density Functional Theory and Experimental Study. *J. Am. Chem. Soc.* **2017**, *139* (17), 6054−6057.
(38) Cong, M.; Yang, B.; Hong, F.; Zheng, T.; Sang, Y.; Guo, J.; Yang, S.; Han, K. Self-Trapped Exciton Engineering for White-Light Emission in Colloidal Lead-Free Double Perovskite Nanocrystals. *Sci. Bull.* **2020**, *65* (13), 1078−1084.
(39) Li, T.; Zhao, X.; Yang, D.; Du, M. H.; Zhang, L. Intrinsic defect properties in halide double perovskites for optoelectronic applications. *J. Am. Phys. Soc.* **2018**, *10* (4), 041001−041007.
(40) Thawarkar, S.; Rondiya, S. R.; Dzade, N. Y.; Khupse, N.; Jadkar, S. Experimental and Theoretical Investigation of the Structural and Opto-Electronic Properties of Fe-Doped Lead-Free Cs2AgBiCl6 Double Perovskite. *Chem.−Eur. J.* **2021**, *27* (26), 7408−7417.
(41) Ahmed, G. H.; El-Demellawi, J. K.; Yin, J.; Pan, J.; Velusamy, D. B.; Hedhili, M. N.; Alarousu, E.; Bakr, O. M.; Alshareef, H. N.; Mohammed, O. F. Giant Photoluminescence Enhancement in CsPbCl3 Perovskite Nanocrystals by Simultaneous Dual-Surface Passivation. *ACS Energy Lett.* **2018**, *3* (10), 2301−2307.
(42) Yong, Z. J.; Guo, S. Q.; Ma, J. P.; Zhang, J. Y.; Li, Z. Y.; Chen, Y. M.; Zhang, B. B.; Zhou, Y.; Shu, J.; Gu, J. L.; Zheng, L. R.; Bakr, O. M.; Sun, H. T. Doping-Enhanced Short-Range Order of Perovskite Nanocrystals for Near-Unity Violet Luminescence Quantum Yield. *J. Am. Chem. Soc.* **2018**, *140* (31), 9942−9951.
(43) Zhang, W.; Wei, J.; Gong, Z.; Huang, P.; Xu, J.; Li, R.; Yu, S.; Cheng, X.; Zheng, W.; Chen, X. Unveiling the Excited-State Dynamics of Mn2+ in 0D Cs4PbCl6 Perovskite Nanocrystals. *Advanced Science* **2020**, *7* (22), 2002210.
(44) Meng, W.; Wang, X.; Xiao, Z.; Wang, J.; Mitzi, D. B.; Yan, Y. Parity-Forbidden Transitions and Their Impact on the Optical Absorption Properties of Lead-Free Metal Halide Perovskites and Double Perovskites. *J. Phys. Chem. Lett.* **2017**, *8* (13), 2999−3007.
(45) Smith, M. D.; Karunadasa, H. I. White-Light Emission from Layered Halide Perovskites. *Acc. Chem. Res.* **2018**, *51* (3), 619−627.
(46) Ghosh, S.; Shi, Q.; Pradhan, B.; Kumar, P.; Wang, Z.; Acharya, S.; Pal, S. K.; Pullerits, T.; Karki, K. J. Phonon Coupling with Excitons and Free Carriers in Formamidinium Lead Bromide Perovskite Nanocrystals. *J. Phys. Chem. Lett.* **2018**, *9* (15), 4245−4250.
(47) Yang, B.; Hong, F.; Chen, J.; Tang, Y.; Yang, L.; Sang, Y.; Xia, X.; Guo, J.; He, H.; Yang, S.; Deng, W.; Han, K. Colloidal Synthesis and Charge-Carrier Dynamics of $Cs_2AgSb_{1-y}Bi_yX_6$ (X: Br, Cl; $0 \leq y \leq 1$) Double Perovskite Nanocrystals. *Angew. Chem., Int. Ed.* **2019**, *58* (8), 2278−2283.
(48) Ke, B.; Zeng, R.; Zhao, Z.; Wei, Q.; Xue, X.; Bai, K.; Cai, C.; Zhou, W.; Xia, Z.; Zou, B. Homo- and Heterovalent Doping-Mediated Self-Trapped Exciton Emission and Energy Transfer in Mn-Doped $Cs_2Na_{1-x}Ag_xBiCl_6$ Double Perovskites. *J. Phys. Chem. Lett.* **2020**, *11* (1), 340−348.
(49) Leveillee, J.; Volonakis, G.; Giustino, F. Phonon-Limited Mobility and Electron-Phonon Coupling in Lead-Free Halide Double Perovskites. *J. Phys. Chem. Lett.* **2021**, *12* (18), 4474−4482.
(50) Maughan, A. E.; Ganose, A. M.; Bordelon, M. M.; Miller, E. M.; Scanlon, D. O.; Neilson, J. R. Defect Tolerance to Intolerance in the Vacancy-Ordered Double Perovskite Semiconductors Cs2SnI6 and Cs2TeI6. *J. Am. Chem. Soc.* **2016**, *138* (27), 8453−8464.
(51) Liu, M.; Zhong, G.; Yin, Y.; Miao, J.; Li, K.; Wang, C.; Xu, X.; Shen, C.; Meng, H. Aluminum-Doped Cesium Lead Bromide Perovskite Nanocrystals with Stable Blue Photoluminescence Used for Display Backlight. *Advanced Science* **2017**, *4* (11), 1700335.
(52) Mondal, N.; De, A.; Samanta, A. Achieving Near-Unity Photoluminescence Efficiency for Blue-Violet-Emitting Perovskite Nanocrystals. *ACS Energy Lett.* **2019**, *4* (1), 32−39.
(53) Liao, Q.; Chen, J.; Zhou, L.; Wei, T.; Zhang, L.; Chen, D.; Huang, F.; Pang, Q.; Zhang, J. Z. Bandgap Engineering of Lead-Free Double Perovskite Cs2AgInCl6Nanocrystals via Cu2+-Doping. *J. Phys. Chem. Lett.* **2020**, *11* (19), 8392−8398.
(54) Appadurai, T.; Chaure, S.; Mala, M.; Chandiran, A. K. Role of Copper in Enhancing Visible Light Absorption in Cs2Ag(Bi, In, Sb)Cl6Halide Double-Perovskite Materials. *Energy Fuel.* **2021**, *35* (14), 11479−11487.
(55) Bhat, M. A.; Ingole, P. P.; Chaudhari, V. R.; Haram, S. K. Outer Sphere Electroreduction of CCl_4 in 1-Butyl-3- Methylimmidazolium Tetrafluoroborate: An Example of Solvent Specific Effect of Ionic Liquid. *J. Phys. Chem. B* **2009**, *113* (9), 2848−2853.
(56) Wadhai, S.; Jadhav, Y.; Thakur, P. Synthesis of Metal-Free Phosphorus Doped Graphitic Carbon Nitride-P_{25} (TiO_2) Composite: Characterization, Cyclic Voltammetry and Photocatalytic Hydrogen Evolution. *Sol. Energy Mater. Sol. Cells* **2021**, *223*, 110958.
(57) Rondiya, S. R.; Buldu, D. G.; Brammertz, G.; Jadhav, Y. A.; Cross, R. W.; Ghosh, H. N.; Davies, T. E.; Jadkar, S. R.; Dzade, N. Y.; Vermang, B. Revealing the Electronic Structure, Heterojunction Band Offset and Alignment of Cu2ZnGeSe4: A Combined Experimental and Computational Study towards Photovoltaic Applications. *Phys. Chem. Chem. Phys.* **2021**, *23* (15), 9553−9560.
(58) Kresse, G.; Hafner, J. Ab Initio Molecular Dynamics for Liquid Metals. *Phys. Rev. B* **1993**, *47* (1), 558−561.
(59) Kresse, G.; Joubert, D. From Ultrasoft Pseudopotentials to the Projector Augmented-Wave Method. *Phys. Rev. B: Condens. Matter Mater. Phys.* **1999**, *59* (3), 1758−1775.
(60) Kresse, G.; Furthmüller, J. Efficient Iterative Schemes for Ab Initio Total-Energy Calculations Using a Plane-Wave Basis Set. *Phys. Rev. B: Condens. Matter Mater. Phys.* **1996**, *54* (16), 11169−11186.
(61) Perdew, J. P.; Burke, K.; Ernzerhof, M. Generalized Gradient Approximation Made Simple. *Phys. Rev. Lett.* **1996**, *77* (18), 3865−3868.
(62) Blöchl, P. E. Projector Augmented-Wave Method. *Phys. Rev. B* **1994**, *50* (24), 17953−17979.
(63) Grimme, S.; Antony, J.; Ehrlich, S.; Krieg, H. A Consistent and Accurate Ab Initio Parametrization of Density Functional Dispersion Correction (DFT-D) for the 94 Elements H-Pu. *J. Chem. Phys.* **2010**, *132* (15), 154104.
(64) Krukau, A. V.; Vydrov, O. A.; Izmaylov, A. F.; Scuseria, G. E. Influence of the Exchange Screening Parameter on the Performance of Screened Hybrid Functionals. *J. Chem. Phys.* **2006**, *125* (22), 224106.
(65) Tribbey, W. *Numerical Recipes*; Cambridge University Press: New York, 2010; Vol. 35, pp 30−31..
(66) Pack, J. D.; Monkhorst, H. J. "special Points for Brillouin-Zone Integrations"-a Reply. *Phys. Rev. B* **1977**, *16* (4), 1748−1749.

https://doi.org/10.1021/acsphyschemau.4c00008
ACS Phys. Chem Au 2024, 4, 476−489